

Multipassage Landau-Zener tunneling oscillations in transverse/longitudinal dual dressing of atomic qubits

Alessandro Fregosi¹, Carmela Marinelli^{2,1}, Carlo Gabbanini¹, Valerio Biancalana², Maria Allegrini^{3,4}, Ennio Arimondo^{3,1}, Francesco Petiziol⁵, Sandro Wimberger^{6,7}, Andrea Fioretti¹, and Giuseppe Bevilacqua^{2,*}

¹INO-CNR, Via G. Moruzzi 1, 56124 Pisa, Italy

²Dipartimento di Scienze Fisiche, della Terra e dell'Ambiente, Università degli Studi di Siena, Via Roma 56, 53100 Siena, Italy

³Dipartimento di Fisica E. Fermi, Università of Pisa, Largo B. Pontecorvo 3, 56127 Pisa, Italy

⁴NEST, Istituto Nanoscienze CNR, Piazza S. Silvestro 12, 56127 Pisa, Italy

⁵Technische Universität Berlin, Institut für Physik und Astronomie, Hardenbergstraße 36, 10623 Berlin, Germany

⁶Department of Mathematical, Physical and Computer Sciences, University of Parma, Parco Area delle Scienze 7/A, 43124, Parma, Italy

⁷National Institute for Nuclear Physics (INFN), Milano Bicocca Section, Parma Group, Parco Area delle Scienze 7/A, 43124, Parma, Italy

*bevilacqua@unisi.it

ABSTRACT

We investigate the time evolution of a non-resonant dressed-atom qubit in an XZ original configuration. It is composed of two electromagnetic fields, one oscillating parallel and the other orthogonal to the quantisation magnetic static field. The experiments are performed in rubidium and caesium atomic magnetometers, confined in a magneto-optical trap and in a vapour cell, respectively. Static fields in the μT range and kHz oscillating fields with large Rabi frequencies are applied. This dual-dressing configuration is an extension of the Landau-Zener multipassage interferometry in the presence of an additional dressing field controlling the tunneling process by its amplitude and phase. Our measurement of the qubit coherence introduces additional features to the transition probability readout of standard interferometry. The coherence time evolution is characterized by oscillations at several frequencies, each of them produced by a different quantum contribution. Such frequency description introduces a new picture of the qubit multipassage evolution. Because the present low-frequency dressing operation does not fall within the standard Floquet engineering paradigm based on the high-frequency expansion, we develop an ad-hoc dressing perturbation treatment. Numerical simulations support the adiabatic and non-adiabatic qubit evolution.

Introduction

Floquet engineering is a vital technique for analyzing quantum systems influenced by periodic electromagnetic fields, allowing the generation of unique quantum properties across various domains, including physics, chemistry, and engineering¹⁻⁵. It captures the dynamics of time-dependent Hamiltonians through effective Hamiltonians that account for the system's key features, characterized by two distinct time evolutions: a micromotion, which occurs at the frequency of the periodic field, and a slower evolution governed by the effective Hamiltonian.

The experimental approach to a Floquet engineered system typically isolates the slower dynamics by integrating the faster, less relevant one, often eliminating the need for a detailed integration due to the small amplitude of the micromotion. This capability is advantageous for quantum simulation tasks, such as those involving cold atomic gases⁶⁻¹² and solid state ones¹³⁻¹⁵. There, the intricacies of the micromotion can be neglected to focus on the emergent phenomena captured by the effective Hamiltonian.

We present here experimental and theoretical studies on the strong periodic bi-modal nonresonant drive of a two-level atomic qubit, which fits within the broader context of two-level systems influenced by virtual/real photons^{16,17}. This concept, initially proposed by Cohen-Tannoudji and Haroche^{18,19}, focuses on an energy splitting that is small relative to the driving field's frequency. In the Floquet framework, the effective Hamiltonian accounts for an energy splitting modulated by the dressing field amplitude. Previous work^{20,21} exploring dual-dressing with two electromagnetic fields of different polarizations

has provided insight into how these dual interactions can yield new dynamical behaviours and effective Hamiltonians that significantly modify the system's energy landscape. Several original features are introduced into the present dual dressing study.

In our configuration, an atomic qubit with energy splitting produced by a static magnetic field is dressed by oscillating fields with frequencies lower than the qubit's Larmor precession frequency and large amplitudes. Here, the dynamics unfolds a fast timescale diverging from the standard Floquet treatment that, unlike previous studies indicating adiabatic behaviour in slow driving regimes⁴, allows us to explore non-adiabatic features. Our focus on quantum control involves direct measurement of the qubit time evolution, revealing a distinct spin evolution that deviates from traditional micromotion patterns.

The XZ dual-dressing setup utilizes the interaction of atomic qubits with two off-resonant magnetic fields, namely an x -axis oscillating field and a z -axis oscillating one periodically adjusting the magnetic energy gap. XZ dual dressing of a two-level system was proposed in Refs. 22, 23 within the context of nonadiabatic dynamics acceleration. This configuration implements a periodic multi-passage scheme akin to the Landau-Zener-Stückelberg-Majorana (LZSM) interferometer, as reviewed in Ref. 24, 25, examined in solid state experiments^{26–28} and planned in optical lattice clocks²⁹. Our experimental approach enhances LZSM studies by detecting the transverse oscillating spin component rather than the conventional probability transfer between eigenstates. The relative phase of the driving fields regulating the periodicity of the multi-passage tunneling and the continuous monitoring represent additional LZSM handles. The strong nonlinear response of the spin dynamics produces high-order interference oscillations with their collapse and revival at different time periods. The direct detection of the qubit full wave function, including its phase, is important nowadays for quantum control and quantum information, as pointed out in Ref. 30.

Operating at high electromagnetic field strengths, our system deviates from the rotating-wave approximation, used typically in LZSM analyses. For a two level driven system the electromagnetic field strength is usually measured by the ratio between the Rabi frequency of the electromagnetic drive and the Larmor frequency. While experiments with a pulsed laser excitation hardly account phase relations, continuous-wave experiments mitigate these concerns. This was demonstrated in prior works^{31–35} exploring Rabi frequencies up to four times the Larmor frequency, with the highest values reached inside a cavity as in Ref. 36. In this work we employ Rabi frequencies up to seven times larger than the Larmor frequency, significantly enhancing quantum control capabilities.

The experiments, exploiting the setups of the previous investigation of the XY dual dressing on both cesium and rubidium atoms,^{20, 37, 38} are briefly described in Section “The qubit system and its detection”. Here, we also present the basic Hamiltonian and some typical evolutions of the system. The full theoretical description, presented in Section “Theoretical treatment” is based on several tools. For the low magnetic fields of our explorations, the atoms are equivalent to an assembly of one-half spins. Owing to the reversed role of our dressing/Larmor frequencies, the standard Floquet high-frequency expansion (HFE) approach cannot be applied. Therefore, we present theoretical descriptions based on i) a full adiabatic evolution valid for weak dressing parameters, ii) a quasi-adiabatic evolution leading to an analytical solution for the spin's time evolution, and iii) a modified Floquet treatment. Numerical simulations describe the strong field dynamics. The connection with the Stückelberg oscillations and other LZSM features is emphasized. The experiments monitor the time dependence of the atomic spin evolution and access the phase of its wavefunction. Several recorded atomic evolutions are presented. Section “LZSM data analysis” discusses the interpretation of our results and the theoretical comparison to the experimental findings. The “Conclusion” Section completes our work.

The qubit system and its detection

Hamiltonian

The time evolution of an assembly of atomic non-interacting qubits in a dual dressing configuration is explored as in Fig. 1, i.e., in the presence of a static magnetic field B_{0z} parallel to the z -axis and two non-resonant electromagnetic fields oscillating at ω angular frequency. For the XZ dressing these fields are oriented along the x and z axes, with B_i the maximum value for $i = (x, z)$. Similar results are obtained in the equivalent YZ dressing configuration. At the applied magnetic fields the atomic structure of rubidium/caesium atoms can be described by a collection of degenerate two-level systems, representing the qubits.

The qubit-field coupling is determined by the $\gamma = g\mu_B$ constant with g an effective Landé factor and μ_B the Bohr magneton, assuming $\hbar = 1$. The spin-static field interaction corresponds to the $\omega_{0z} = \gamma B_{0z}$ Larmor frequency. The coupling with the XZ dressing fields is described by the Rabi frequency amplitudes $\Omega_x = \gamma B_x$ and $\Omega_z = \gamma B_z$, respectively. Introducing Φ_{0z} , the phase difference between x and z dressings, the XZ Hamiltonian is written as

$$H(t) = \frac{1}{2}\vec{h}(t) \cdot \vec{\sigma}, \quad (1)$$

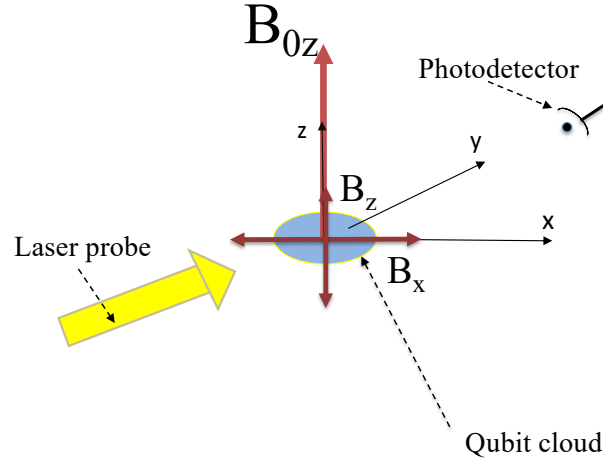


Figure 1. Schematic of a qubit dressed by the B_x and B_z oscillating fields, generated by the radiofrequency coils and in the presence of a B_{0z} static field. In this figure the $\langle \sigma_y(t) \rangle$ expectation value is monitored by the polarization rotation of a probe beam propagating along the y axis.

with the effective $\vec{h}(t)$ field given by

$$\vec{h}(t) = \begin{pmatrix} \Omega_x \cos(\omega t) \\ 0 \\ \omega_{0z} + \Omega_z \cos(\omega t + \Phi_{0z}) \end{pmatrix}. \quad (2)$$

Owing to negligible decoherence processes this Hamiltonian is complete. Starting from the initial $\langle \sigma_x(t=0) \rangle = 1$ qubit coherence, the time evolution of the $\langle \sigma_x(t) \rangle$ coherence, or of the equivalent one along the y axis, is monitored in the experiment. The theory comparison requires the control of the following parameters: the oscillation frequency ω , the bare Larmor angular frequency ω_{0z} , the Ω_x , (transverse) and the Ω_z (longitudinal) Rabi angular frequencies, all expressed in kHz units in the following, and the Φ_{0z} phase. As for our $\omega \ll \omega_{0z}, \Omega_x, \Omega_z$ operational parameters the standard dressed atom HFE approach used in Floquet engineering is not suitable, we rely on various theoretical treatments: 1) an adiabatic one, improved by non-adiabatic corrections, 2) a perturbative approach in a suitable rotating frame owing to the large Ω_z/ω ratio, and finally 3) numerical simulations.

We notice that the above XZ bichromatic driving Hamiltonian, which reduces to the LZSM one for $\Omega_z = 0$, represents a very rich configuration to explore. A LZSM $\Omega_z = 0$ scheme with Z-axis bichromatic driving was explored in Ref. 39.

Experimental setup and results

We perform our observations in two experimental setups: a first one where an ^{85}Rb atomic sample is laser-cooled and trapped in a magneto-optical trap to a few tens of micro-Kelvins, occupying the single $F_g = 3$ hyperfine state⁴⁰, and a second apparatus that employs ^{133}Cs atoms contained in a vapor cell and prepared in the $F_g = 4$ hyperfine state⁴¹. In the Rb case, the cold atomic sample is monitored during its 10 ms free-fall and exhibits a damped dynamics with a characteristic time of about 4 ms. In the Cs case, a vapor sample in 23 Torr buffer gas contained in a centimetric cell is interrogated after being optically laser pumped, and the signal damping lasts about 10 ms. Both experiments work in cycles: in a first phase atoms are prepared spin-polarized along the x -axis using a circularly polarized pump laser in the presence of a uniform B_{0z} static magnetic field. At the conclusion of the polarization phase, two radiofrequency fields, linearly polarized and operating in the 1-10 kHz range with amplitudes varying from 0 to 50 μT , are applied to the atoms along the (x, z) or (y, z) directions. The time scale of dressing evolution refers to the zero initial phase choice of the effective field, as described in Eq. (2).

The expectation value of $\langle \sigma_y(t) \rangle$ for Rb and $\langle \sigma_x(t) \rangle$ for Cs is monitored by examining the polarization rotation (Faraday effect) of a probe beam propagating along the y or x -axis, respectively, as depicted in Fig. 1.

The rotation angle, from the initial direction to the final orientation, is analyzed with a balanced polarimeter, whose output enables a precise detection of the amplitude and phase of the magnetization component along the monitored axis. In both cases the measured Faraday rotation signal is renormalized to compensate for the signal decay. The time resolution is limited

by the sampling rate which is 250 kHz and 125 kHz in the Rb and in the Cs cases, respectively. The Rb experiment uses crossed laser beams for the pumping and probe purposes, both tuned to the $D2$ line of Rb (780 nm), while the Cs one uses two co-propagating laser beams tuned to $D1$ (pump, 895 nm) and $D2$ (probe, 852 nm) lines of Cs. In the cesium case the pump component is detuned several GHz out of resonance during the measurement and finally filtered away before the polarimeter while it is just cut off in the rubidium experiment.

Some measured time dependencies of the atomic spin evolution are illustrated in Fig. 2, with Rabi frequency values increasing from left to right. The balanced polarimeter output is plotted against the reduced time $\tau = t/T$, where $T = 2\pi/\omega$ represents the radiofrequency field period, and $\tau = 0$ corresponds to the initial preparation state $\langle \sigma_x \rangle = 1$. The plots of this Figure offer a synthetic overview for all recorded temporal structures. The spin component aligned with the detection axis oscillates quasi-periodically between positive and negative values, produced by spin precession in the (x, y) horizontal plane. The recorded signals exhibit three distinct periodic or quasi-periodic patterns. The first precise periodicity matches the dressing fields' period T , corresponding to $\Delta\tau$ integer values. The other two patterns are shorter period structures, appearing quasi-regular in (a) and chirped in frequency in (b), that reflect the large amplitude oscillations of the qubit coherence. The amplitude of those oscillations is time modulated with the T period. At high dressing frequencies Ω_x or Ω_z , the oscillation pattern repeats with a substantial $\Delta\tau$ period, 3.00(1) for the parameters in plot (c). Similar experimental results are presented in Fig 3(a).

For the parameters in Fig. 2(c), the ratio between Rabi frequency and atomic splitting is 7.4. Experiments with ratios up to 10 showed a comparably long periodicity. For comparison we notice that the continuous-wave, strong-drive experiment in Ref. 34 applied Rabi frequencies up to four times the Larmor frequency.

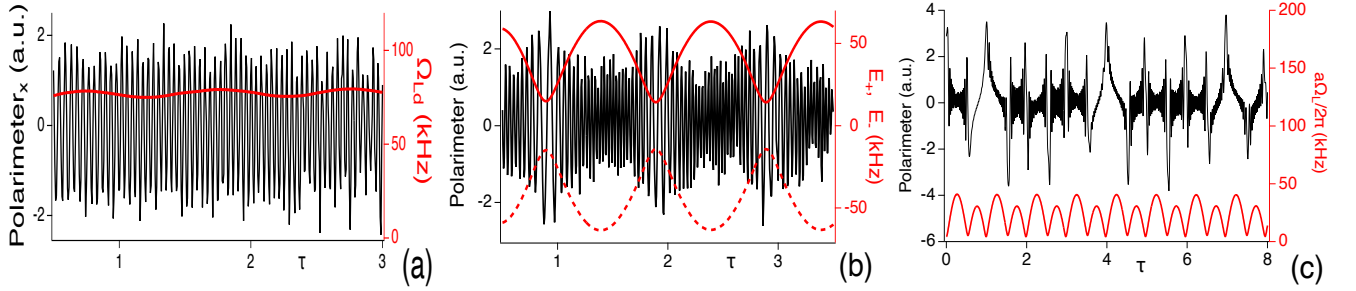


Figure 2. (Color online) Time evolution of the atomic spin. Black lines (left axis) report experimental polarimeter signals, red lines (right axis) the theoretical Ω_{Ld} of Eq. (3) derived from the applied static and oscillating field values. On the horizontal axis the τ reduced time. Parameters $(\omega, \omega_{0z}, \Omega_x, \Omega_z)$ all in kHz and Φ_{0z} . In (a) Rb atoms, (3.0, 77.645, 2.06, 2.0) and $\Phi_{0z} = 0$, a linearly polarized oscillating field; in (b) Rb atoms, (3.0, 77.645, 53.1, 146.9) and $\Phi_{0z} = \pi/2$; in (c) Cs atoms, (1.028, 4.42, 6.27, 31.79) and $\Phi_{0z} = 0.70\pi$. For the (c) parameters the large value of the Z dressing amplitude leads to two maxima and minima within each time period of the effective field. Note the different time periodicity.

Theoretical treatment

Our theoretical analysis of the qubit response follows different action lines. The numerical solution of the Schrödinger equation for the $|\psi\rangle$ wavefunction represents the most precise approach. That solution handles also the more general case of an initial $t = 0$ qubit preparation not matching the zero phase of the x -axis driving as in the effective field of Eq. (2). Numerical solutions of the Schrödinger equation are presented in Figs. 3(b)-(d), and 5. The numerical solutions, representing the key element for the analysis of the experimental data, point out the high sensitivity of the qubit time evolution to dressing parameters and initial conditions. Both elements limit the accuracy of the experiment-theory comparison.

Within an adiabatic approach, the qubit time evolution is determined by the time-periodic $(E_+(t), E_-(t))$ eigenvalues of the XZ Hamiltonian of Eq. (1). These eigenvalues are derived from the \hbar modulus as follows:

$$\Omega_{Ld}(t) = \hbar = \sqrt{\Omega_x^2 \cos(\omega t)^2 + [\omega_{0z} + \Omega_z \cos(\omega t + \Phi_{0z})]^2}, \quad (3a)$$

$$E_+(t) = -E_-(t) = \frac{\Omega_{Ld}}{2}. \quad (3b)$$

with the time-dependent Ω_{Ld} dressed atom Larmor frequency corresponding to the dressed-atom energy gap at time t . Ω_{Ld} is equivalent to the Rabi oscillation frequency of LZSM theory/experiment^{28,42}. The time dependence of the Ω_{Ld} Larmor dressed frequency are represented by continuous red lines in several plots. In Fig. 2(a) where the dressing amplitudes are very low

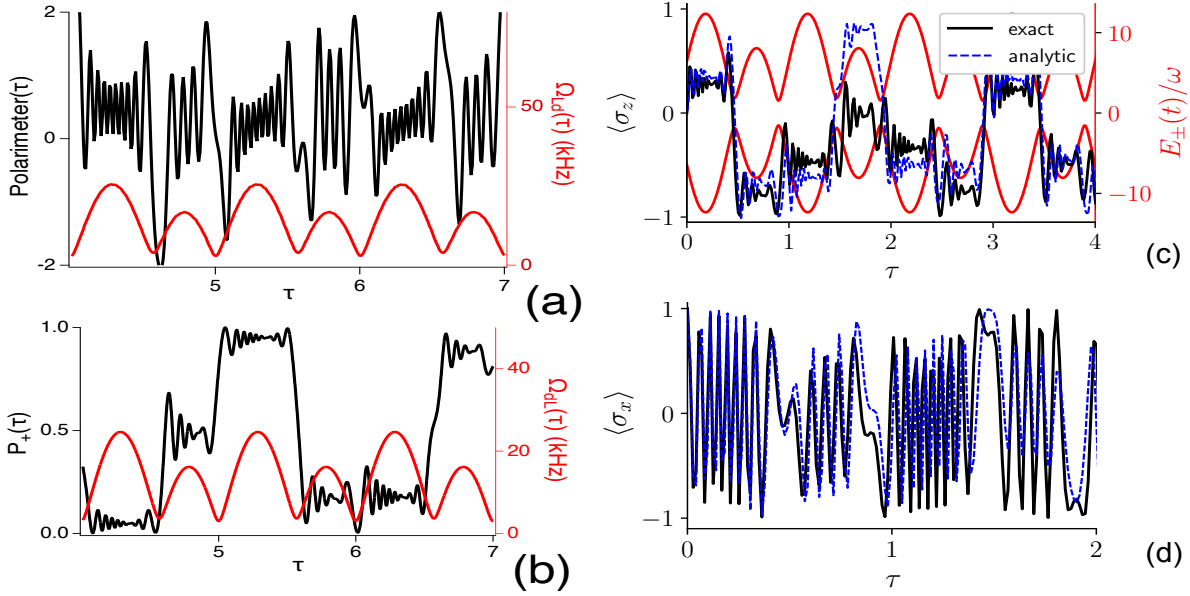


Figure 3. (Color online) Left column: in (a) black line experimental polarimeter signal and in (b) P_+ probability occupation of the $|+\rangle$ eigenstate derived from numerical solution of the Schrödinger equation as function of the $\tau = \omega t / (2\pi)$ reduced time. Red lines: in the time dependence of the Ω_{Ld} Larmor dressed frequency. Right column: comparison between the exact numerical time evolution and the analytical estimate [see the main text and Appendix “Model for the low-frequency nonadiabatic regime”] based on the modified Floquet approach. Cs parameters in kHz: $\omega = 1.028$, $\omega_{0z} = 4.42$, $\Omega_x = 3.85$, and $\Omega_z = 20.93$, and $\Phi_{0z} = 1.63\pi$ corresponding to a nonadiabatic regime. Notice that for these parameters the large value of the Z dressing amplitude leads to two maxima and minima within each time period of the effective field.

Ω_{Ld} is almost constant, dominated by the ω_{0z} static contribution. In Fig. 2(b), at increased dressing amplitude, the modulated component acquires a larger weight. Here, the time evolution of the eigenenergies is characterized by a sequence of avoided crossings with T periodicity. For the Fig. 2(c) plot parameters, corresponding to even larger modulation amplitude, the dual dressing operation leads to two separated avoided crossings within a single T period.

An adiabatic perturbation treatment is valid for a slowly-changing time-dependent Hamiltonian, as recalled in Appendix “Adiabatic perturbation theory”. It is applied in Appendix “XZ rotating Hamiltonian” to a simplified XZ excitation scheme, denoted as rotating XZ, where $\Omega_x = \Omega_z$ and $\Phi = \pi/2$. This analysis shows that the evolution of the monitored spin components depends on two parameters: the $\theta(t)$ orientation angle of the \vec{h} vector and the LZSM interference phase $\phi(t)$ given by

$$\begin{aligned}\theta(t) &= \arctan\left(\frac{h_x}{h_z}\right) = \arctan\left(\frac{\Omega_x \cos(\omega t)}{\omega_{0z} + \Omega_z \cos(\omega t + \Phi_{0z})}\right), \\ \phi(t) &= \int_0^t \Omega_{Ld}(\tau) d\tau.\end{aligned}\quad (4)$$

A similar geometric approach based on a rotation around an axis in the xy plane followed by a rotation around the z -axis was explored for a standard LZSM evolution in Ref. 24.

As in Eq. (35) the time dependence of the $\langle \sigma_x(t) \rangle, \langle \sigma_y(t) \rangle$ spin mean values is given by

$$\begin{aligned}\langle \sigma_x(t) \rangle &\propto \cos(\phi), \\ \langle \sigma_y(t) \rangle &\propto \sin(\phi).\end{aligned}\quad (5)$$

These expressions, verified numerically, evidence the key role played by the Ω_{Ld} frequency into the time-dependent spin mean values. The qubit oscillation at the Ω_{Ld} Larmor angular frequency of Eq. (3) produces the ϕ accumulated phase. The $\theta(t)$ orientation angle determines the amplitude of the qubit oscillations monitored along the experimental detection axis. The observed complex qubit oscillating response is based on the Ω_{Ld} time dependent fast oscillations combined with a slower scale variations of the amplitude variations. Additional interference oscillations are produced by the multi-passage LZSM avoided crossings, as shown in the following Section.

To describe the nonadiabatic low-frequency regime for our $\omega \ll \omega_{0z}$ operation, the standard HFE Floquet approach is

not appropriate. Hence, a perturbative dressed atom approach is developed here. The spirit of this approach is to derive a perturbative expansion in the limit of large Ω_z^{-1} . As detailed in Appendix “Model for the low-frequency nonadiabatic regime”, this is achieved by representing the problem in a time-dependent rotating frame where the Fourier components of the Hamiltonian are proportional to $\sim \Omega_x J_n(\Omega_z/\omega)$, where $J_n(\cdot)$ are Bessel functions of the first kind. The small value of the latter for large values of the argument Ω_z/ω , as compared to the value of Ω_x considered, justifies an expansion of the effective Floquet Hamiltonian H_{eff} and the Floquet kick operator $K(t)$ (Appendix “Model for the low-frequency nonadiabatic regime”). This provides an approximation of the evolution operator in the form of Floquet’s theorem

$$U(t, t_0) = e^{-iK(t)} e^{-iH_{\text{eff}}(t-t_0)} e^{iK(t_0)}. \quad (6)$$

As shown in Fig. 3 (c)-(d), this approach succeeds in capturing the key features of the exact dynamics with a second-order description also in the low-frequency, but yet nonadiabatic, regime considered.

LZSM data analysis

In a double Landau-Zener tunneling process, with an avoided crossing region passed twice at the same speed, the excitation probability becomes an oscillating function characterized by the so-called Stückelberg oscillations. In a multi-passage Landau-Zener passage the quantum-mechanical interference for the amplitudes of quantum states sequentially mixed at separated crossings leads to additional structures in the qubit time-evolution. In the absence of the Ω_z dressing the Hamiltonian of Eq. (1) reduces to the LZSM one^{24,25}, with the Ω_x driving producing the avoided-crossing sequence. The Ω_z coupling presence modifies the LZSM tunneling process owing to the time dependent orientation angle of the periodic magnetic structures in the qubit time-evolution.

The LZSM tunneling treatment is characterized by different operation regimes, denoted as adiabatic and nonadiabatic ones. For $\Omega_z = 0$ the LZSM derivation of those regimes requires $\omega\Omega_x$ smaller or larger than ω_{0z}^2 , respectively²⁴. For $\Omega_z \neq 0$, a modification of that treatment leads to

$$\omega\sqrt{\Omega_x^2 + \Omega_z^2} \lesseqgtr \omega_{0z}^2. \quad (7)$$

for adiabatic and nonadiabatic evolutions, respectively.

The nonadiabatic tunneling enhances the interference oscillations in the occupation probabilities of the $|\pm\rangle$ states. Those oscillations appear in the P_+ numerical simulation of Figs. 3 (b) and (c) for nonadiabatic parameters. The overall occupation time dependence agrees with previous LZSM work. The probability steps of our simulations correspond to the Landau-Zener crossing processes at the minima of the energy gap, visible in the red lines depicting the adiabatic potentials in Fig. 2. Those jumps are followed by Stückelberg oscillations. These oscillations with a quasi regular frequency match the high frequency ones appearing in all the $\langle\sigma_x\rangle$ plots of Fig. 2. Such matching of the Stückelberg oscillations applies to all our theoretical plots. These nearly periodic oscillations do not appear in previous Stückelberg results, for instance from atom optics interferometry of Refs. 43–45. This quasi-periodicity arises because the ω rate of the Landau-Zener tunneling is small compared to the Stückelberg oscillation frequency.

Our detection of the qubit coherences leads to time dependencies greatly different from the LZSM transition probabilities. The greater contribution to the coherence oscillation is at the $\Omega_{Ld}(\tau)$ frequency and this frequency describes also the probability oscillations. As in Fig. 2(a) at low dressing values the qubit spin performs a precession on a nearly horizontal plane at a quasi constant Ω_{Ld} Larmor dressed frequency. In those conditions the transition probability does not contain $\Omega_{Ld}(\tau)$ frequency components. At larger Ω_z values the Landau-Zener tunneling takes place in the presence of a modification of the precession axis leading to Ω_{Ld} components also into P_+ probabilities.

In order to characterize the qubit response at the $\Omega_{Ld}(\tau)$ frequency, we measure the $t_P(j)$ times corresponding to the j -th zero signal values of the polarimeter. For those times the qubit spin orientation is orthogonal to the monitored axis. The time separation between neighbouring zero values represents the period time for a single Larmor precession. From the measured times we derive the experimental dressed Larmor frequency $f_{Ld}(j)$ at the time $t_j = [t_P(j) + t_P(j+1)]/2$ given by

$$f_{Ld}(j) = \frac{2\pi}{t_P(j+1) - t_P(j)}. \quad (8)$$

Fig. 4 reports measured f_{Ld} time evolutions of the dressed qubit frequency for several dressing parameters. The (a) plot evidences the f_{Ld} time periodicity with the dressing period T . Owing to such periodicity all the f_{Ld} values may be folded back into a single $(0, 1)$ time period. Within the temporal analog of real-space periodic Hamiltonian of Ref. 46, that folding represents a reduction to a single Floquet zone corresponding to the Bloch zone for periodicity in position space for our time periodicity. $f_{Ld}(t)$ folded plots are reported in Fig. 4(b) and (c). Fig. 4(d) reports a case where the f_{Ld} vs τ is not fully periodic,

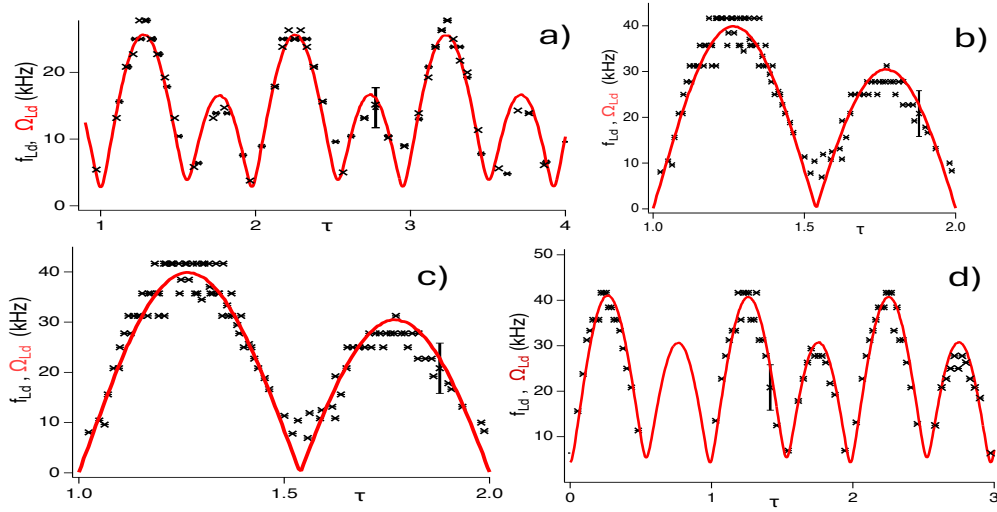


Figure 4. (Color online) Measured f_{Ld} and predicted Ω_{Ld} values for time dependent adiabatic frequency versus time. Frequencies in kHz and times τ in reduced units. f_{Ld} frequencies (black squares) are derived from the polarimeter zero values as in Eq. (8). The typical error bars, reported for clarity only for one/two points in each plot, are determined by the sampling rate, leading to larger errors at closely spaced time intervals and higher f_{Ld} values. In (b) and (c) plots the f_{Ld} high value data are discrete because of the limited sampling rate. Red lines Ω_{Ld} report theoretical values calculated from Eq. (3). Notice that no adjustable parameters are introduced in the calculation. Parameters ($\omega, \omega_{0z}, \Omega_x, \Omega_z$) frequencies in kHz and Φ_{0z} : in (a) Cs 1.028, 4.42, 3.85, 20.93, and 1.63π as in Fig. 3; in (b) Rb experiment 3.0, 77.645, 51.56, 96.77, and $\pi/2$; in (c) Cs (1.03, 4.66, 4.55, 35.3) and 0; in (d) Cs atoms, (1.028, 4.42, 6.27, 31.79) and 0.70π , as in Fig. 2c).

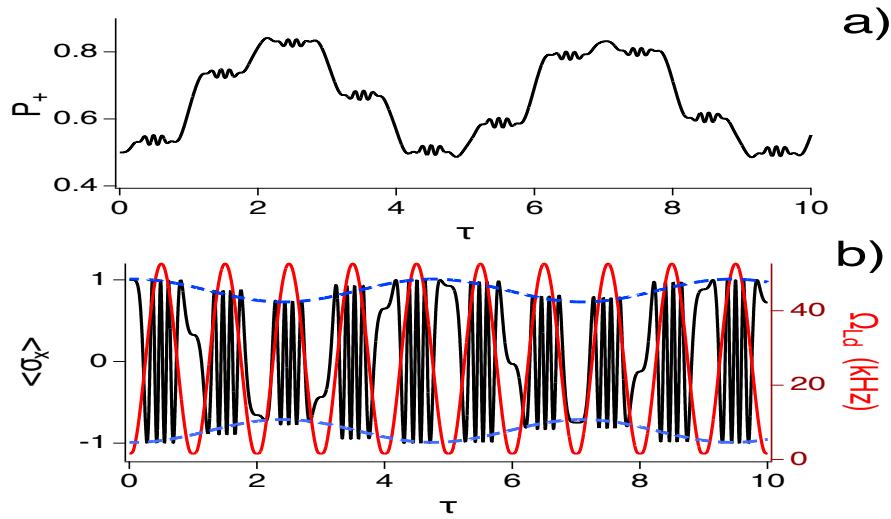


Figure 5. (Color online) Theoretical simulation of the Rabi-like oscillations with initial $\langle \sigma_x(0) \rangle = 1$. In a) $P_+(\tau)$ occupation probability and in b) $\langle \sigma_x(\tau) \rangle$. Blue dashed lines are fits of the Rabi-like oscillations with 4.61τ oscillation period and the $\Omega_{Rl} = 0.213$ kHz frequency. For the coherence in b) the Rabi-like oscillations masked by the large amplitude of the Larmor dressed oscillations produce an amplitude modulation of the Ω_{Ld} oscillations. Parameters in kHz: (1., 4.197, 0.254, 4.189), and $\Phi_{0z} = \pi$.

as examined in the following paragraph. The f_{Ld} measured values are compared to the time dependent $\Omega_{Ld}(\tau)$, showing a remarkable agreement limited by the time resolution of the sampling acquisition rate. The wavefunction interferences

associated to multiple periodic Landau-Zener processes introduce additional periodic oscillating structures, for the $\Omega_z = 0$ LZSM discussed theoretically in Refs. 24, 42 and investigated in solid-state experiments^{28, 47, 48}. In these works, focused on the occupation probabilities, such periodic structures are denominated Rabi-like oscillations with their Ω_{RI} frequency approximated by the Ω_z dressing frequency^{29, 42, 49}. The Rabi-like positive and negative interferences appear also for our Hamiltonian as in the simulations of Fig. 5 with the $P_+(\tau)$ occupation probability in (a) and the $\langle \sigma_x(\tau) \rangle$ coherence in (b). Rabi-like oscillations are clearly visible in the occupation probability. The Larmor dressed frequency oscillations produce the high-frequency modulation of the $P_+(\tau)$ envelope. For the coherence the Rabi-like oscillations produce an amplitude modulation of the Larmor dressed frequency oscillations. Their experimental detection is limited by our sampling resolution. The Rabi-like oscillations well resolved in the data of Fig. 2(c) produce a periodic large modification of the coherence time dependence. Their presence leads to the absence of data points in the f_{Ld} vs τ plot of Fig. 4(d) for τ in the (0.49, 1.06) interval, with $4.13(2)\tau$ oscillation period, corresponding to 0.25 kHz. The experimental results for the Rabi-like oscillations are described by numerical simulations. Their dependence on the Hamiltonian parameters appears more complex than the theoretical ones for the standard LZSM single dressing process.

Conclusion

The time evolution of an atomic qubit interacting with two off-resonant dressing fields in a longitudinal/transversal configuration is examined experimentally. The qubit coherence is recorded for long interaction times with negligible relaxation processes on the evolution timescales. The standard Floquet engineering treatment predicts a time evolution with a constant dressed Larmor frequency, not matching these experimental results owing to our dressing parameters. We develop a theoretical analysis relying on numerical simulations combined to an adiabatic treatment and an ad-hoc dressed-atom perturbation treatment. An analytical formula for the frequency of the Rabi-like oscillations will be an useful tool. The complex mathematical treatment for the $\Omega_z = 0$ of Refs. 29, 42, 49 evidences a hard task to complete. Our longitudinal/transversal dressing configuration represents an extended version of the multi-passage LZSM tunneling, with the transverse dressing modifying the tunneling probability. An important feature of the present experiment is the continuous monitoring of the qubit coherences, which gives a direct access to the phase wavefunction and opens new perspectives in the LZSM quantum control. In terms of the Bloch vector evolution, the transition probability monitors its z component while the coherences monitor the evolution within the xy plane. The time evolution of the latter shows the presence of several frequency contributions: the dressing one, the dressed Larmor one and the Rabi-like one. Within the time dependent transition probability, the dressed Larmor frequency components produce Stückelberg oscillations, which represent a single component of the total evolution. On the contrary, those oscillations dominate the coherence time evolution. The probability evolution represents a strong probe of the Rabi-like oscillations.

Our work opens a new exploration direction within the broad area of LZSM interferometry. The ability to control the dynamics of the atomic qubit in this dual-dressing regime expands the toolbox for quantum state manipulation. Alternative fast quantum logic gates using nonadiabatic LZSM transitions were introduced in Ref. 50 and similar shortcuts to adiabaticity in Refs. 22, 23. Our experimental investigation evidencing the rich dynamics associated to the XZ configuration opens an avenue to quantum control accelerations.

Appendices

Adiabatic perturbation theory

Following the treatment of 51, 52, the adiabatic perturbation theory comes into play when the Hamiltonian is slowly changing in time, i.e., we replace $t \rightarrow \epsilon t$ where $\epsilon \ll 1$ and $1/\epsilon$ represents the slow characteristic time scale.

Let us consider a time dependent Hamiltonian $H(t)$ with its $G(t)$ diagonalizing unitary operator

$$G^\dagger(t)H(t)G(t) = H_D(t) \quad (9)$$

H_D has a diagonal form with $E_i(t)$ instantaneous eigenvalues. The Schrödinger equation ($\hbar = 1$) for the time evolution operator $U(t)$

$$i\dot{U}(t) = H(t)U(t) \quad U(0) = 1 \quad (10)$$

is rewritten in an adiabatic picture introducing

$$U_G(t) = G^\dagger(t)U(t)G(0) \quad (11)$$

which satisfies

$$i\dot{U}_G(t) = [H_D(t) + i\dot{G}^\dagger(t)G(t)]U_G(t) \quad U_G(0) = 1 \quad (12)$$

Introducing $\tau = \varepsilon t$ with $d/dt = \varepsilon d/d\tau$, the last equation is rewritten as

$$iU'_G(\tau) = [\varepsilon^{-1}H_D(\tau) + i(G^\dagger(\tau))'G(\tau)]U_G(\tau), \quad (13)$$

where we have introduced $f'(\tau) = df(\tau)/d\tau$. The r.h.s. first term represents the largest H_D contribution. We rewrite the r.h.s. second term as

$$i[G^\dagger(\tau)]'G(\tau) \equiv V_D(\tau) + V_{ND}(\tau) \quad (14)$$

separating the V_D diagonal part related to the Berry phase from the V_{ND} non-diagonal part. Separating the diagonal and not-diagonal contributions, the U_G evolution operator is given by

$$iU'_G(\tau) = \left[\underbrace{\varepsilon^{-1}H_D(\tau) + V_D(\tau)}_{\text{diagonal}} + \underbrace{V_{ND}(\tau)}_{\text{not-diagonal}} \right] U_G(\tau), \quad (15)$$

By defining the $Q(\tau)$ operator as the integral of the diagonal part

$$Q(\tau) \equiv \int_0^\tau [\varepsilon^{-1}H_D(\tau) + V_D(\tau)]d\tau, \quad Q(0) = 0, \quad (16)$$

we introduce the $U_{G,I}(\tau)$ adiabatic-interaction time evolution operator

$$U_G(\tau) = e^{-iQ(\tau)}U_{G,I}(\tau), \quad U_{G,I}(0) = 1. \quad (17)$$

We obtain

$$\begin{aligned} i(U_{G,I})' &= e^{iQ(\tau)}V_{ND}(\tau)e^{-iQ(\tau)}U_{G,I}(\tau) \\ &\equiv \tilde{V}_{ND}(\tau)U_{G,I}(\tau) \end{aligned} \quad (18)$$

to be solved perturbatively. The potential \tilde{V}_{ND} induces transitions between the eigenstates $|E_i(\tau)\rangle$, neglected in the $\varepsilon \rightarrow 0$ adiabatic limit.

At the lowest perturbation order, equivalent to the adiabatic theorem, setting $U_{G,I}(\tau) \approx 1$ we neglect the $\tilde{V}_{ND}(\tau)$ contribution in Eq. (17) obtaining

$$U_G(\tau) \approx e^{-iQ(\tau)}. \quad (19)$$

The approximated time-evolution operator results

$$U(\tau) \approx G(\tau)U_G(\tau)G^\dagger(0) = G(\tau)e^{-iQ(\tau)}G^\dagger(0) \quad (20)$$

XZ rotating Hamiltonian

Let us consider a simplified XZ excitation scheme, denoted as rotating XZ, where $\Omega_x = \Omega_z = \Omega$ and the x,z dressing components with Φ phase shift. The Hamiltonian is given by

$$H = \frac{1}{2} [\Omega \sin(\omega t + \Phi) \sigma_x + (\omega_{0z} + \Omega \cos(\omega t + \Phi)) \sigma_z]. \quad (21)$$

with the \vec{h}^R effective field, equivalent of Eq. (3), given by

$$\vec{h}^R = \begin{pmatrix} \Omega \sin(\omega t + \Phi) \\ 0 \\ \omega_{0z} + \Omega \cos(\omega t + \Phi) \end{pmatrix}. \quad (22)$$

Let's define

$$m = \frac{\omega_{0z}}{\Omega} \quad (23)$$

and introduce the h^R modulus and the θ^R vector orientation angle,

$$h^R(t) \equiv \Omega \sqrt{1 + 2m \cos(\omega t + \Phi) + m^2} \quad (24a)$$

$$\theta^R(t) \equiv \arctan\left(\frac{h_x^R}{h_z^R}\right) = \arctan\left(\frac{\sin(\omega t + \Phi)}{m + \cos(\omega t + \Phi)}\right), \quad (24b)$$

this last one equivalent to the θ orientation angle of Eq. (4). The rotating Hamiltonian of Eq. (21) rewritten as

$$H = \frac{h^R}{2} [\cos \theta^R \sigma_z + \sin \theta^R \sigma_x] \quad (25)$$

is diagonalized by the following G operator representing a rotation around the y axis:

$$G = e^{-i\theta^R(t) \sigma_y/2}. \quad (26)$$

The diagonalized H_D Hamiltonian results

$$H_D = G^\dagger(t)H(t)G(t) = \frac{h^R(t)}{2} \sigma_z \quad (27)$$

with the r.h.s. of Eq. (13) given by Eq. (14) becomes here

$$i\dot{G}^\dagger G = -\frac{1}{2} \theta^R(\tau)' \sigma_y = V_{ND} \quad (28)$$

consisting only of off-diagonal terms.

Introducing an adimensional time

$$\tau = \frac{\omega t}{2\pi} \equiv \varepsilon t \quad \omega \approx 0 \quad (29)$$

the previous Eq. (15) becomes

$$i(U_G(\tau))' = \frac{1}{2} \left[\frac{2\pi}{\omega} h^R \sigma_z + \theta^R(\tau)' \sigma_y \right] U_G(\tau). \quad (30)$$

We introduce the $\phi(\tau)$ time accumulated phase angle of the main text Eq. (4)

$$\begin{aligned} \phi(\tau) &= \frac{2\pi}{\omega} \int_0^\tau h^R(\tau) d\tau \\ &= \frac{2\pi}{\omega} \Omega \int_0^\tau \sqrt{1 + 2m \cos(2\pi\tau + \Phi) + m^2} d\tau, \end{aligned} \quad (31)$$

where the integral can be expressed through a second kind elliptic integral. Then, we obtain for the Q operator

$$Q(\tau) = \frac{1}{2} \phi(\tau) \sigma_z, \quad (32)$$

and for the time evolution operator in the lowest order

$$U(\tau) = e^{-i\theta(\tau) \sigma_y/2} e^{-i\Phi(\tau) \sigma_z/2} e^{i\theta(0) \sigma_y/2}. \quad (33)$$

Using this operator, the σ_i time evolution is given by

$$\sigma_i(\tau) = U^\dagger(\tau) \sigma_i U(\tau). \quad (34)$$

Introducing $\theta_0 \equiv \theta(0)$ for the initial orientation angle of the effective field, with the system at time $t = \tau = 0$ prepared in the $\sigma_x|\psi\rangle = |\psi\rangle$ eigenstate, we obtain for the expected values $\langle \psi | \sigma_i(\tau) | \psi \rangle \equiv \langle \sigma_i(\tau) \rangle$

$$\begin{aligned} \langle \sigma_x(\tau) \rangle &= \sin(\theta) \sin(\theta_0) + \cos(\theta) \cos(\phi) \cos(\theta_0) \\ \langle \sigma_y(\tau) \rangle &= \cos(\theta_0) \sin(\phi) \\ \langle \sigma_z(\tau) \rangle &= \cos(\theta) \sin(\theta_0) - \sin(\theta) \cos(\phi) \cos(\theta_0), \end{aligned} \quad (35a)$$

with the $\phi(\tau)$ phase angle defined by Eq. (31) for the XZ rotating Hamiltonian, and the equivalent definition in the main text.

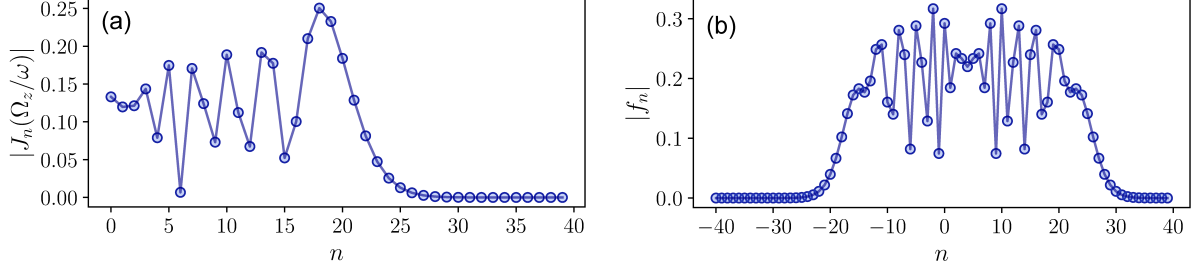


Figure 6. (a) Absolute value of the Bessel functions $J_n(\Omega_z/\omega)$ entering the Fourier coefficients of $H''(t)$ of Eq. (41). (b) Fourier coefficients of $f(t)$ of Eq. (42).

Model for the low-frequency nonadiabatic regime

In this Appendix, an analytical approximation for the dynamics in the low driving frequency, strong z -dressing regime of Fig. 3 (c) - (d) is derived, whose parameters are reported here for convenience (in kHz):

$$\omega/2\pi = 1.028, \quad \omega_{0z}/2\pi = 4.42 \quad (36)$$

$$\Omega_x/2\pi = 3.85, \quad \Omega_z/2\pi = 20.93. \quad (37)$$

This regime is not well captured neither by an adiabatic approximation (for which ω is not small enough) nor by a conventional Floquet high-frequency expansion (for which ω is not large enough). However, the fact that Ω_z is substantially larger than other parameters can still be used to construct a perturbative expansion, in a suitable transformed frame, which well approximates the dynamics. The transformed frame is defined by two steps. First, since the qubit splitting ω_{0z} is close in value to four driving quanta ω , a rotating frame oscillating at frequency 4ω is chosen. This is defined by the unitary

$$V(t) = e^{-i(4\omega)t\sigma_z/2} \quad (38)$$

and the transformed-frame Hamiltonian $H' = V^\dagger H V - iV^\dagger \partial_t V$ reads as

$$H'(t) = \frac{\delta}{2} \sigma_z + \frac{\Omega_x}{2} \cos(\omega t) (e^{i4\omega t} \sigma_+ + e^{-i4\omega t} \sigma_-) + \frac{\Omega_z}{2} \cos(\omega t + \Phi_{0z}) \sigma_z, \quad (39)$$

with $\delta = \omega_{0z} - 4\omega$. The second step is to integrate out (choose a frame co-rotating with) the z -dressing field, via the transformation

$$V'(t) = \exp\left(-i\frac{\Omega_z}{2} \int_0^t dt' \cos(\omega t' + \Phi_{0z}) \sigma_z\right) \quad (40a)$$

$$= \exp\left(-i\frac{\Omega_z}{2\omega} [\sin(\omega t + \Phi_{0z}) - \sin(\Phi_{0z})] \sigma_z\right). \quad (40b)$$

Note that, although we found conceptually more clear to introduce the two steps $V(t)$ and $V'(t)$ separately, they commute with each other and, thus, they can be straightforwardly combined into a single transformation. The transformed Hamiltonian $H'' = (V')^\dagger H' V' - i(V')^\dagger \partial_t V'$ is given by

$$H''(t) = \frac{\delta}{2} \sigma_z + \frac{\Omega_x}{2} \cos(\omega t) \times \left(e^{i4\omega t + i(\Omega_z/2)[\sin(\omega t + \Phi_{0z}) - \sin(\Phi_{0z})]} \sigma_+ + \text{H.c.} \right). \quad (41)$$

By expanding the exponentials via Bessel functions⁵³, H'' can finally be rewritten as

$$H''(t) = \frac{\delta}{2} \sigma_z + \frac{\Omega_x}{4} f(t) \sigma_+ + \frac{\Omega_x}{4} f^*(t) \sigma_-, \quad (42)$$

where $f(t) = \sum_{n=-\infty}^{\infty} f_n \exp(in\omega t)$ has Fourier components

$$f_n = \left[J_{n-5} \left(\frac{\Omega_z}{\omega} \right) e^{-i5\Phi_{0z}} + J_{n-3} \left(\frac{\Omega_z}{\omega} \right) e^{-i3\Phi_{0z}} \right] \times e^{in\Phi_{0z}} e^{-i\Omega_z \sin(\Phi_{0z})/\omega}. \quad (43)$$

The Fourier components of H'' , defined by $H'' = \sum_{n=-\infty}^{+\infty} H_n \exp(in\omega t)$, can thus be identified as

$$H_n = \frac{\delta}{2} \sigma_z \delta_{n,0} + \frac{\Omega_x}{4} [f_n \sigma_+ + f_{-n}^* \sigma_-], \quad (44)$$

with f_n given in Eq. (43). In the transformed frame, we are still dealing with a time-periodic Hamiltonian at frequency ω [Eq. (41)]. However, since the Bessel functions have small value for large argument Ω_z/ω , the advantage of the transformed frame is that the coefficients of H_n have now small magnitude as compared to ω (differently from the lab-frame Hamiltonian). This is illustrated quantitatively in Fig. 6, where the values of $|J_n(\Omega_z/\omega)|$ and $|f_n|$ are reported for the parameter values of interest of Fig. 3. Provided $\Omega_x/\Omega_z \ll 1$ and $\delta/\Omega_z \ll 1$, this allows one to construct a perturbative expansion with standard methods. In particular, the dynamics $U''(t)$ generated by $H''(t)$ can then be estimated by using Floquet's theorem³⁻⁵,

$$U''(t) = e^{-iK(t)} e^{-iH_{\text{eff}}(t-t_0)} e^{iK(t_0)}, \quad (45)$$

and a Floquet inverse-frequency expansion for the effective Hamiltonian H_{eff} and kick operator $K(t)$ ³⁻⁵. To second-order, this is computed from the Fourier components H_n of Eqs. (44) and (43) according to⁵

$$H_{\text{eff}} \simeq H_0 + \frac{1}{\omega} \sum_{n=1}^{\infty} \frac{1}{n} [H_n, H_{-n}] \quad (46)$$

$$K(t) \simeq -\frac{i}{\omega} \sum_{n \neq 0} \frac{H_n}{n} e^{in\omega t} + \frac{i}{\omega^2} \sum_{n \neq 0} \left(\frac{[H_0, H_n]}{n^2} e^{in\omega t} + \sum_{m \neq 0, n} \frac{[H_{-m}, H_n]}{2n(n-m)} e^{i(n-m)\omega t} \right). \quad (47)$$

Note, once more, that the small parameter justifying the expansion is not the inverse frequency ω^{-1} , but rather (the matrix elements of) H_n . The lab-frame evolution $U(t)$ is finally obtained as

$$U(t) = V(t) V'(t) U''(t) \quad (48)$$

from Eqs. (38) and (40a). Since both $V'(t)$ and $V''(t)$ are ω -periodic, they can be absorbed into the micromotion operator, such that Eqs. (48) and (45) straightforwardly define a Floquet-type decomposition also in the lab frame. Given that the parameters of Fig. 3 satisfy the condition $\Omega_x/\Omega_z \ll 1$ and $\delta/\Omega_z \ll 1$, which underlie the expansion, quite approximately, it is to be expected that a satisfactory description requires beyond-first-order terms in the expansion. We find that a second-order truncation already reproduces fairly well the exact dynamics.

References

1. Shirley, J. H. Solution of the Schrödinger equation with a Hamiltonian periodic in time. *Phys. Rev.* **138**, B979–B987, DOI: [10.1103/PhysRev.138.B979](https://doi.org/10.1103/PhysRev.138.B979) (1965).
2. Sambe, H. Steady states and quasienergies of a quantum-mechanical system in an oscillating field. *Phys. Rev. A* **7**, 2203–2213, DOI: [10.1103/PhysRevA.7.2203](https://doi.org/10.1103/PhysRevA.7.2203) (1973).
3. Goldman, N. & Dalibard, J. Periodically driven quantum systems: Effective Hamiltonians and engineered gauge fields. *Phys. Rev. X* **4**, 031027, DOI: [10.1103/PhysRevX.4.031027](https://doi.org/10.1103/PhysRevX.4.031027) (2014).
4. Bukov, M., D'Alessio, L. & Polkovnikov, A. Universal high-frequency behavior of periodically driven systems: from dynamical stabilization to Floquet engineering. *Adv. Phys.* **64**, 139–226 (2015).
5. Eckardt, A. Colloquium: Atomic quantum gases in periodically driven optical lattices. *Rev. Mod. Phys.* **89**, 011004, DOI: [10.1103/RevModPhys.89.011004](https://doi.org/10.1103/RevModPhys.89.011004) (2017).
6. Aidelsburger, M. *et al.* Realization of the Hofstadter Hamiltonian with ultracold atoms in optical lattices. *Phys. Rev. Lett.* **111**, 185301, DOI: [10.1103/PhysRevLett.111.185301](https://doi.org/10.1103/PhysRevLett.111.185301) (2013).
7. Meinert, F., Mark, M. J., Lauber, K., Daley, A. J. & Nägerl, H.-C. Floquet engineering of correlated tunneling in the Bose-Hubbard model with ultracold atoms. *Phys. Rev. Lett.* **116**, 205301, DOI: [10.1103/PhysRevLett.116.205301](https://doi.org/10.1103/PhysRevLett.116.205301) (2016).
8. Geier, S. *et al.* Floquet Hamiltonian engineering of an isolated many-body spin system. *Science* **374**, 1149–1152, DOI: [10.1126/science.abd9547](https://doi.org/10.1126/science.abd9547) (2021).
9. Weitenberg, C. & Simonet, J. Tailoring quantum gases by Floquet engineering. *Nat. Phys.* **17**, 1342–1348, DOI: [10.1038/s41567-021-01316-x](https://doi.org/10.1038/s41567-021-01316-x) (2021).

10. Scholl, P. *et al.* Microwave engineering of programmable XXZ Hamiltonians in arrays of Rydberg atoms. *PRX Quantum* **3**, 020303, DOI: [10.1103/PRXQuantum.3.020303](https://doi.org/10.1103/PRXQuantum.3.020303) (2022).
11. Yin, M.-J. *et al.* Floquet engineering Hz-level Rabi spectra in shallow optical lattice clock. *Phys. Rev. Lett.* **128**, 073603, DOI: [10.1103/PhysRevLett.128.073603](https://doi.org/10.1103/PhysRevLett.128.073603) (2022).
12. Zhang, J.-Y. *et al.* Tuning anomalous Floquet topological bands with ultracold atoms. *Phys. Rev. Lett.* **130**, 043201, DOI: [10.1103/PhysRevLett.130.043201](https://doi.org/10.1103/PhysRevLett.130.043201) (2023).
13. Salathé, Y. *et al.* Digital quantum simulation of spin models with circuit quantum electrodynamics. *Phys. Rev. X* **5**, 021027, DOI: [10.1103/PhysRevX.5.021027](https://doi.org/10.1103/PhysRevX.5.021027) (2015).
14. Mahmood, F. *et al.* Selective scattering between Floquet-Bloch and Volkov states in a topological insulator. *Nat. Phys.* **12**, 306, DOI: [10.1038/nphys3609](https://doi.org/10.1038/nphys3609) (2016).
15. Peng, P., Yin, C., Huang, X., Ramanathan, C. & Cappellaro, P. Floquet prethermalization in dipolar spin chains. *Nat. Phys.* **17**, 444–447, DOI: [10.1038/s41567-020-01120-z](https://doi.org/10.1038/s41567-020-01120-z) (2021).
16. Allegrini, M. & Arimondo, E. Atoms dressed by virtual and real photons. *Physics* **6**, 60–74, DOI: [10.3390/physics6010005](https://doi.org/10.3390/physics6010005) (2024).
17. Passante, R. & Rizzuto, L. Vacuum self-dressing of an atom and its physical effects. *doi: 10.20944/preprints202503.1700.v1* (2025).
18. Haroche, S., Cohen-Tannoudji, C., Audoin, C. & Schermann, J. P. Modified Zeeman hyperfine spectra observed in H^1 and Rb^{87} ground states interacting with a nonresonant rf field. *Phys. Rev. Lett.* **24**, 861, DOI: [10.1103/PhysRevLett.24.861](https://doi.org/10.1103/PhysRevLett.24.861) (1970).
19. Haroche, S. & Cohen-Tannoudji, C. Resonant transfer of coherence in nonzero magnetic field between atomic levels of different g factors. *Phys. Rev. Lett.* **24**, 974–978, DOI: [10.1103/PhysRevLett.24.974](https://doi.org/10.1103/PhysRevLett.24.974) (1970).
20. Bevilacqua, G., Biancalana, V., Vigilante, A., Zanon-Willette, T. & Arimondo, E. Harmonic fine tuning and triaxial spatial anisotropy of dressed atomic spins. *Phys. Rev. Lett.* **125**, 093203, DOI: [10.1103/PhysRevLett.125.093203](https://doi.org/10.1103/PhysRevLett.125.093203) (2020).
21. Bevilacqua, G., Biancalana, V., Zanon-Willette, T. & Arimondo, E. Harmonic dual dressing of spin-1/2 systems. *Phys. Rev. A* **105**, 022619, DOI: [10.1103/PhysRevA.105.022619](https://doi.org/10.1103/PhysRevA.105.022619) (2022).
22. Petiziol, F., Dive, B., Mintert, F. & Wimberger, S. Fast adiabatic evolution by oscillating initial hamiltonians. *Phys. Rev. A* **98**, 043436, DOI: [10.1103/PhysRevA.98.043436](https://doi.org/10.1103/PhysRevA.98.043436) (2018).
23. Petiziol, F., Mintert, F. & Wimberger, S. Quantum control by effective counterdiabatic driving. *Europhys. Lett.* **145**, 15001, DOI: [10.1209/0295-5075/ad19e3](https://doi.org/10.1209/0295-5075/ad19e3) (2024).
24. Shevchenko, S., Ashhab, S. & Nori, F. Landau–Zener–Stückelberg interferometry. *Phys. Reports* **492**, 1–30, DOI: <https://doi.org/10.1016/j.physrep.2010.03.002> (2010).
25. Ivakhnenko, O. V., Shevchenko, S. N. & Nori, F. Nonadiabatic Landau–Zener–Stückelberg–Majorana transitions, dynamics, and interference. *Phys. Reports* **995**, 1–89, DOI: <https://doi.org/10.1016/j.physrep.2022.10.002> (2023).
26. Oliver, W. D. *et al.* Mach-Zehnder interferometry in a strongly driven superconducting qubit. *Science* **310**, 1653–1657, DOI: [10.1126/science.1119678](https://doi.org/10.1126/science.1119678) (2005).
27. Sillanpää, M., Lehtinen, T., Paila, A., Makhlin, Y. & Hakonen, P. Continuous-time monitoring of Landau-Zener interference in a Cooper-pair box. *Phys. Rev. Lett.* **96**, 187002, DOI: [10.1103/PhysRevLett.96.187002](https://doi.org/10.1103/PhysRevLett.96.187002) (2006).
28. Zhou, J. *et al.* Observation of time-domain Rabi oscillations in the Landau-Zener regime with a single electronic spin. *Phys. Rev. Lett.* **112**, 010503, DOI: [10.1103/PhysRevLett.112.010503](https://doi.org/10.1103/PhysRevLett.112.010503) (2014).
29. Liu, W.-X., Wang, T., Zhang, X.-F. & Li, W.-D. Time-domain Landau-Zener–Stückelberg–Majorana interference in an optical lattice clock. *Phys. Rev. A* **104**, 053318, DOI: [10.1103/PhysRevA.104.053318](https://doi.org/10.1103/PhysRevA.104.053318) (2021).
30. Kofman, P. O., Ivakhnenko, O. V., Shevchenko, S. N. & Nori, F. Majorana’s approach to nonadiabatic transitions validates the adiabatic-impulse approximation. *Sci. Reports* **13**, 5033, DOI: [10.1038/s41598-023-31084-y](https://doi.org/10.1038/s41598-023-31084-y) (2023).
31. Fuchs, G. D., Dobrovitski, V. V., Toyli, D. M., Heremans, F. J. & Awschalom, D. D. Gigahertz dynamics of a strongly driven single quantum spin. *Science* **326**, 1520–1522, DOI: [10.1126/science.1181193](https://doi.org/10.1126/science.1181193) (2009).
32. Tuorila, J. *et al.* Stark effect and generalized Bloch–Siegert shift in a strongly driven two-level system. *Phys. Rev. Lett.* **105**, 257003, DOI: [10.1103/PhysRevLett.105.257003](https://doi.org/10.1103/PhysRevLett.105.257003) (2010).

33. Scheuer, J. *et al.* Precise qubit control beyond the rotating wave approximation. *New J. Phys.* **16**, 093022, DOI: [10.1088/1367-2630/16/9/093022](https://doi.org/10.1088/1367-2630/16/9/093022) (2014).
34. Avinadav, C., Fischer, R., London, P. & Gershoni, D. Time-optimal universal control of two-level systems under strong driving. *Phys. Rev. B* **89**, 245311, DOI: [10.1103/PhysRevB.89.245311](https://doi.org/10.1103/PhysRevB.89.245311) (2014).
35. Deng, C., Orgiazzi, J.-L., Shen, F., Ashhab, S. & Lupascu, A. Observation of Floquet states in a strongly driven artificial atom. *Phys. Rev. Lett.* **115**, 133601, DOI: [10.1103/PhysRevLett.115.133601](https://doi.org/10.1103/PhysRevLett.115.133601) (2015).
36. Langford, N. K. *et al.* Experimentally simulating the dynamics of quantum light and matter at deep strong coupling. *Nat. Commun.* **8**, 1715, DOI: [10.1038/s41467-017-01061-x](https://doi.org/10.1038/s41467-017-01061-x) (2017).
37. Fregosi, A. *et al.* Floquet space exploration for the dual-dressing of a qubit. *Sci. Reports* **13**, 15304 (2023).
38. Bevilacqua, G., Biancalana, V., Dancheva, Y. & Fregosi, A. Tri-axial time-dependent magnetic field calibrated in-situ by harmonic analysis of adiabatically evolving atomic spins (2025). [2404.14574](https://doi.org/10.26434/chemrxiv-2025-14574).
39. Forster, F. *et al.* Landau-Zener interference at bichromatic driving. *Phys. Rev. B* **92**, 245422, DOI: [10.1103/PhysRevB.92.245422](https://doi.org/10.1103/PhysRevB.92.245422) (2015).
40. Fregosi, A. *et al.* Magnetic induction imaging with a cold-atom radio frequency magnetometer. *Appl. Phys. Lett.* **117**, 144102, DOI: [10.1063/5.0020415](https://doi.org/10.1063/5.0020415) (2020).
41. Bevilacqua, G., Biancalana, V., Dancheva, Y. & Vigilante, A. Sub-millimetric ultra-low-field MRI detected in situ by a dressed atomic magnetometer. *Appl. Phys. Lett.* **115**, 174102, DOI: [10.1063/1.5123653](https://doi.org/10.1063/1.5123653) (2019).
42. Ashhab, S., Johansson, J. R., Zagoskin, A. M. & Nori, F. Two-level systems driven by large-amplitude fields. *Phys. Rev. A* **75**, 063414, DOI: [10.1103/PhysRevA.75.063414](https://doi.org/10.1103/PhysRevA.75.063414) (2007).
43. Kling, S., Salger, T., Grossert, C. & Weitz, M. Atomic Bloch-Zener oscillations and Stückelberg interferometry in optical lattices. *Phys. Rev. Lett.* **105**, 215301, DOI: [10.1103/PhysRevLett.105.215301](https://doi.org/10.1103/PhysRevLett.105.215301) (2010).
44. Zenesini, A., Ciampini, D., Morsch, O. & Arimondo, E. Observation of Stückelberg oscillations in accelerated optical lattices. *Phys. Rev. A* **82**, 065601, DOI: [10.1103/PhysRevA.82.065601](https://doi.org/10.1103/PhysRevA.82.065601) (2010).
45. Rahman, T. *et al.* Bloch oscillation phases investigated by multipath Stückelberg atom interferometry. *Phys. Rev. Res.* **6**, L022012, DOI: [10.1103/PhysRevResearch.6.L022012](https://doi.org/10.1103/PhysRevResearch.6.L022012) (2024).
46. Martin, I., Refael, G. & Halperin, B. Topological frequency conversion in strongly driven quantum systems. *Phys. Rev. X* **7**, 041008, DOI: [10.1103/PhysRevX.7.041008](https://doi.org/10.1103/PhysRevX.7.041008) (2017).
47. Berns, D. M. *et al.* Amplitude spectroscopy of a solid-state artificial atom. *Nature* **455**, 51–57, DOI: [10.1038/nature07262](https://doi.org/10.1038/nature07262) (2008).
48. Yang, Z.-X. *et al.* Phase-sensitive Landau-Zener-Stückelberg interference in superconducting quantum circuit*. *Chin. Phys. B* **30**, 024212, DOI: [10.1088/1674-1056/abd753](https://doi.org/10.1088/1674-1056/abd753) (2021).
49. Neilinger, P. *et al.* Landau-Zener-Stückelberg-Majorana lasing in circuit quantum electrodynamics. *Phys. Rev. B* **94**, 094519, DOI: [10.1103/PhysRevB.94.094519](https://doi.org/10.1103/PhysRevB.94.094519) (2016).
50. Ryzhov, A. I., Ivakhnenko, O. V., Shevchenko, S. N., Gonzalez-Zalba, M. F. & Nori, F. Alternative fast quantum logic gates using nonadiabatic Landau-Zener-Stückelberg-Majorana transitions. *Phys. Rev. Res.* **6**, 033340, DOI: [10.1103/PhysRevResearch.6.033340](https://doi.org/10.1103/PhysRevResearch.6.033340) (2024).
51. Demirplak, M. & Rice, S. A. Assisted adiabatic passage revisited. *J. Phys. Chem. B* **109**, 6838–44, DOI: [10.1021/jp040647w](https://doi.org/10.1021/jp040647w) (2005).
52. Weinberg, P. *et al.* Adiabatic perturbation theory and geometry of periodically-driven systems. *Phys. Reports* **688**, 1–35, DOI: <https://doi.org/10.1016/j.physrep.2017.05.003> (2017).
53. *NIST Digital Library of Mathematical Functions*. <http://dlmf.nist.gov/>, Release 1.0.23 of 2019-06-15 (2019). F. W. J. Olver, A. B. Olde Daalhuis, D. W. Lozier, B. I. Schneider, R. F. Boisvert, C. W. Clark, B. R. Miller and B. V. Saunders, eds.

Acknowledgements

All authors thank D. Petrucci and A. Barbini for technical assistance.

S. W. acknowledges financial support by: Q-DYNAMO (EU HORIZON-MSCA-2022-SE-01) with project No. 101131418. A. Fr. acknowledges the Italian MUR through the PNRR project “EuPRAXIA Advanced Photon Sources (EuAPS)” contract EuAPS IR0000030 CUP I93C21000160006 for the support.

A. Fi. acknowledges financial support from the PNRR MUR project PE0000023-NQSTI financed by the European Union - Next Generation EU

F. P. acknowledges funding from the Deutsche Forschungsgemeinschaft (DFG, German Research Foundation) through the Emmy Noether Programme – project number 555842149.

Author contributions statement

A. Fr., A. Fi., C. G., C. M. and V. B. performed the experiments: E. A., V. B. and A. Fi. conceived the probe tools. A. Fr., V. B. and A. Fi. analysed the results. E. A., M. A., G. B., S. W. and F. P. performed the theoretical analysis. All the authors prepared the manuscript. All authors reviewed the manuscript.